Ice Initiation by Aerosol Particles: Measured and Predicted Ice Nuclei Concentrations versus Measured Ice Crystal Concentrations in an Orographic Wave Cloud

T. Eidhammer,[a,b] P. J. DeMott,[b] A. J. Prenni,[b] M. D. Petters,[b,c] C. H. Twohy,[d] D. C. Rogers,[a]
J. Stith,[a] A. Heymsfield,[a] Z. Wang,[e] K. A. Pratt,[f,g] K. A. Prather,[f] S. M. Murphy,[h,i]
J. H. Seinfeld,[h] R. Subramanian,[j] and S. M. Kreidenweis[a]

[a] National Center for Atmospheric Research,[k] Boulder, Colorado
[b] Department of Atmospheric Science, Colorado State University, Fort Collins, Colorado
[d] Department of Atmospheric and Oceanic Sciences, Oregon State University, Corvallis, Oregon
[e] Department of Atmospheric Science, University of Wyoming, Laramie, Wyoming
[f] Department of Chemistry and Biochemistry, University of California, San Diego, La Jolla, California
[h] Division of Chemistry and Chemical Engineering, California Institute of Technology, Pasadena, California
[j] Droplet Measurement Technologies, Boulder, Colorado

ABSTRACT

The initiation of ice in an isolated orographic wave cloud was compared with expectations based on ice nucleating aerosol concentrations and with predictions from new ice nucleation parameterizations applied in a cloud parcel model. Measurements of ice crystal number concentrations were found to be in good agreement both with measured number concentrations of ice nuclei feeding the clouds and with ice nuclei number concentrations determined from the residual nuclei of cloud particles collected by a counterflow virtual impactor. Using lognormal distributions fitted to measured aerosol size distributions and measured aerosol chemical compositions, ice nuclei and ice crystal concentrations in the wave cloud were reasonably well predicted in a 1D parcel model framework. Two different empirical parameterizations were used in the parcel model: a parameterization based on aerosol chemical type and surface area and a parameterization that links ice nuclei number concentrations to the number concentrations of particles with diameters larger than 0.5 μm. This study shows that aerosol size distribution and composition measurements can be used to constrain ice initiation by primary nucleation in models. The data and model results also suggest the likelihood that the dust particle mode of the aerosol size distribution controls the number concentrations of the heterogeneous ice nuclei, at least for the lower temperatures examined in this case.

1. Introduction

The poorly understood link between aerosol properties and heterogeneous ice nucleation served as a focus of

[c] Current affiliation: Department of Marine, Earth, and Atmospheric Sciences, North Carolina State University, Raleigh, North Carolina.

[g] Current affiliation: Department of Chemistry, Purdue University, West Lafayette, Indiana.

[i] Current affiliation: Chemical Sciences Division, NOAA/Earth System Research Laboratory, Boulder, Colorado.

Corresponding author address: Trude Eidhammer, National Center for Atmospheric Research, 3450 Mitchell Lane, Boulder, CO 80301. E-mail: trude@ucar.edu

the Ice in Clouds Experiment–Layer Clouds (ICE-L). In particular, the ability to predict ice formation on the basis of measured aerosol properties and ice nuclei (IN) number concentrations was the overarching focus of this study. Past studies have indicated that large discrepancies (up to several orders of magnitudes) often exist between measured number concentrations of IN and of ice crystals in nearby clouds (Pruppacher and Klett 1997). Some discrepancies can be explained by secondary ice formation processes such as rime splintering (Hallett and Mossop 1974), but for other cases the cause of the disagreement is unclear (e.g., Prenni et al. 2007). Theories to explain the observed differences have been suggested: for example, freezing by deliquescent cloud condensation nuclei (CCN; Khvorostyanov and Curry 2000, 2004) or primary or secondary nucleation mechanisms that involve freezing of liquid droplets during evaporation or formation of ice

nuclei during the same process (e.g., Cotton and Field 2002; Fridlind et al. 2007). All of these hypotheses remain to be physically tested. However, one factor that has been brought to light in recent years is that many in situ ice crystal measurements from aircraft may have been contaminated by shattering of large ice crystals on the inlets of instruments (e.g., Field et al. 2003; McFarquhar et al. 2007; Jensen et al. 2009), resulting in measurements of unrealistically high concentration of small ice crystals. This finding suggests that the ice nuclei versus ice crystal discrepancy could in many cases be due to measurement artifacts.

The ICE-L field study targeted orographic wave clouds for studying primary ice formation processes. In idealized wave clouds, the airflow is laminar, parcels follow the streamlines, and they spend typically only a few hundred seconds in the cloud. For relatively thin and isolated wave clouds with low ice crystal concentrations, there is minimal ice sedimentation or mixing, so parcel models may be suitable for modeling of ice initiation in these clouds (Sassen and Dodd 1989; Heymsfield and Miloshevich 1993).

In the context of studying aerosol effects on ice initiation and developing a predictive understanding of how changes in aerosol fields lead to changes in cloud properties, it is necessary to account for number concentrations and IN efficiencies of different aerosol types in the atmosphere. Still, many heterogeneous ice nucleation parameterizations relate ice crystal number concentrations simply to supersaturation (e.g., Meyers et al. 1992) or temperature (Cooper 1986; Fletcher 1962) and do not consider any relationship among aerosol number concentrations, physico-chemical properties, and IN. Recently, several different heterogeneous ice nucleation parameterizations have been suggested that take aerosol properties into account (Diehl and Wurzler 2004; Khvorostyanov and Curry 2004; Phillips et al. 2008, hereafter PDA08; Connolly et al. 2009; DeMott et al. 2010, hereafter D10). In a previous study incorporating some of these parameterizations in a detailed microphysical Lagrangian parcel model, it was demonstrated that the semiempirical parameterization of Diehl and Wurzler (2004) and the classical theory formulation of Khvorostyanov and Curry (2004) require additional constraints on predicted IN number concentrations in some situations, so that these do not exceed values representing a reasonably small fraction of the total aerosol number concentrations (Eidhammer et al. 2009). In contrast, the heterogeneous ice nucleation parameterization developed by PDA08 is constrained by field measurements of IN number concentration dependence on aerosol surface area and ice supersaturation; it accounts for the proportion of IN numbers contributed by different aerosol types (mineral dust, black carbon, organic carbon). We therefore use the PDA08 parameterization for wave

cloud parcel simulations and comparisons to data in the present study. Further, D10 recently proposed a parameterization of immersion and condensation freezing nucleation that relates IN number concentrations only to the number concentrations of ambient particles larger than 0.5 μm in diameter and to temperature. This simplified empirical parameterization is based on a large dataset compiled from IN measurements from several studies, including ICE-L. Testing this parameterization also provides a means to examine whether ignoring the chemical speciation of ice nuclei introduces large errors.

Airborne aerosol, microphysical, and thermodynamic measurements for one particular wave cloud case during ICE-L are used in our study. Here we examine the general equivalence of IN number concentrations, both as measured entering the clouds and from evaporated cloud particles selected by a counterflow virtual impactor (CVI), with ice crystal number concentrations. We then use the aerosol data to initialize an adiabatic parcel model for comparisons of predicted IN and ice crystal concentrations to in situ measurements. The specific cloud is an ideal test bed for parcel model simulations because measurements suggest that simplifying assumptions about the dynamical structure of the cloud is justified.

2. Measurement methods

The National Science Foundation (NSF)–National Center for Atmospheric Research (NCAR) C-130 aircraft served as the airborne measurement platform for ICE-L. Measurements were obtained over Colorado and Wyoming in November and December 2007. Instrumentation aboard the C-130 included aerosol sizing and composition instruments, cloud particle instruments, air motion and thermodynamic sensors, and cloud radar and lidar. Cloud hydrometeor instruments included a 2D-C probe [Particle Measuring System (PMS) Inc., Boulder, CO], which was modified by NCAR to provide faster response and more diode array elements than the standard PMS 2D-C design. The modified instrument has a 64-diode array with 25-μm resolution and sizing capability up to 1600 μm. Small hydrometeors such as cloud droplets were measured by an open-path cloud droplet probe [CDP; Droplet Measurement Technologies (DMT), Boulder, CO] that measures particles with diameters in the range of 3–50 μm. Improved inlets and sampling configurations for these instruments have greatly reduced shattering and the associated artifacts. Aerosol number concentration measurements were made using a condensation nuclei counter (CNC; TSI model 3760), which provided total concentrations of particles with diameters >15 nm, and a wingpod-mounted Ultra High Sensitivity Aerosol Spectrometer (UHSAS; Droplet Measurement Technologies) for optical sizing of particles in the

range from 0.075 to 1 μm in diameter. Single particle analyses were performed on ambient aerosols using an aircraft aerosol time-of-flight mass spectrometer (A-ATOFMS), which couples aerodynamic sizing and laser desorption–ionization with dual-polarity time-of-flight mass spectrometry (Pratt et al. 2009a). Electron microscopy analyses were conducted for particles collected onto grids. Mass size distributions of nonrefractory aerosol species (sulfate, nitrate, ammonium, and organics) were measured in real time using an Aerodyne compact time-of-flight aerosol mass spectrometer (C-ToF-AMS) (Drewnick et al. 2005). Black carbon number and mass distributions were measured using a DMT single particle soot photometer (SP2; Schwarz et al. 2006; Baumgardner et al. 2008).

Ice nuclei measurements were made with an airborne version of the Colorado State University continuous flow diffusion chamber (CFDC) model 1H. This instrument is similar to the one described by Rogers et al. (2001), and its configuration is identical to the instruments used in Petters et al. (2009) and Prenni et al. (2009). The key difference from the instrument as described in Rogers et al. (2001) is the implementation of an actively cooled ice saturation section in the lowest third of the chamber, where liquid cloud particles are evaporated to allow clear optical detection of activated ice crystals. After being sampled through the aircraft inlet, the ambient aerosol was passed through an impactor that removes particles larger than 1.5-μm aerodynamic diameter (50% cut size) before being sent to the CFDC. The CFDC exposed the sample to controlled temperatures ($\sim\pm1°C$) and relative humidities ($\sim\pm3\%$) for $\sim$5 s. For this study the conditions in the CFDC were adjusted such that the CFDC processing temperature approximated the ambient or cloud-pass temperature. The processing relative humidity was set between 95% and 103% with respect to water. The relative humidity settings above water saturation promote activation of most CCN into cloud droplets and favor detecting the net impact of deposition, condensation freezing, and immersion freezing nuclei [see Vali (1985) for definitions of the freezing mechanisms]. The setting below water saturation promotes deposition, or possible immersion freezing of haze particles. Assessment of the significance of contact freezing nucleation was limited because of the short CFDC residence times. To assess the maximum potential number of contact freezing nuclei, the CFDC was sometimes operated at temperatures several degrees colder than the ICE-L target clouds, based on hypothesized relationships between contact freezing nuclei concentrations and concentrations of immersion freezing nuclei active at temperatures several degrees colder (Durant and Shaw 2005).

Aerosol and cloud activation probes sampled through different ambient air inlets. The CNC, CFDC, and

ATOFMS sampled from the University of Wyoming forward-facing single-stage diffuser nozzle inlet, ingesting air at a flow rate ($\sim$700 L min^{-1}) that was adjusted to be isokinetic at the tip (heated to $+7°C$ to avoid blocking from rime ice accumulating in regions of supercooled water). The C-ToF-AMS sampled air from a High-Performance Instrumented Airborne Platform for Environmental Research (HIAPER) modular inlet (HIMIL), a flow-through inlet with a diffusing nozzle upstream, a converging nozzle downstream, and a calculated collection efficiency of approximately 75% for 1-μm diameter particles when operated at typical C-130 sampling air speeds ($\sim$150 m s^{-1}). At typical research speeds there should be $\sim$8°C compressional heating of the air in the HIMIL inlet, which may evaporate some volatile components of the aerosol. The SP2 sampled from a rear-facing inlet on the bottom of the plane.

Cloud particles having diameters above $\sim$7 μm were sampled with a counterflow virtual impactor (Noone et al. 1988; Twohy et al. 1997) and then evaporated to permit measurement of cloud particle residual characteristics, as well as to measure condensed water content using a tunable diode laser hygrometer. A two-stage round-jet impactor was designed for making separate collections of particles in two size ranges: 0.11–0.59-μm diameter unit-density particles (0.08–0.42-μm diameter 1.7 g cm^{-3} density particles) and larger particles up to several microns in diameter. Twohy et al. (2010) and Pratt et al. (2009b) provide additional details regarding single particle analyses of CVI residual particles during ICE-L. Additionally, CVI-separated cloud particle residual nuclei were forwarded at times to other instruments, including the CFDC [see Prenni et al. (2007) for a detailed description of the CFDC/CVI interface], ATOFMS, and C-ToF-AMS instruments. At these times, the other measuring systems switched from their respective ambient aerosol inlets to sampling the CVI exit stream. This permitted analyses of particle composition and IN characteristics of particles activated within all-liquid, mixed-phase, and all-ice cloud regions at different times.

The CVI has an enhancement factor for concentrations close to 30. This enhancement reduces measurement uncertainties in the instruments that sample air through the CVI inlet compared to when these instruments sample through the ambient air inlets. This has a major implication for the CFDC cloud measurements during ICE-L. The lower detection limit for the CFDC is close to 0.3 L^{-1} for 5-min sampling periods when on the ambient air inlet (D10), while when sampling through the CVI (in all cloud passes), the lower detection limit in the CFDC is reduced to about 0.01 L^{-1} (D10).

Bulk and environmental probes used in this study included the King liquid water probe (King et al. 1978),

Rosemount Icing Detector (RICE), and two Buck Research 100C cooled mirror hygrometers. Standard C-130 measurements of winds and temperature were also made. Complete details on each of the standard instruments (range, resolution, accuracy, response time) are available online (http://www.eol.ucar.edu/instrumentation/aircraft/C-130/documentation/c-130-investigator-handbook). Additional ICE-L specific measurements are described in Pratt et al. (2009b) and Twohy et al. (2010).

Radar reflectivities were obtained with the zenith view of the University of Wyoming 85-GHz cloud radar (WCR; Pazmany et al. 1994; Damiani and Haimov, 2006; Leon et al. 2006), and the attenuated backscattering power and linear depolarization ratio (both uncalibrated) were measured using the Wyoming cloud lidar (WCL; Wang et al. 2009).

A typical wave cloud measurement series during the ICE-L included assessment of the cloud temperature and equivalent potential temperature θ_e ranges, followed by measurements of aerosol upstream of clouds in clear air, but at the same θ_e corresponding to cloudy parcels. In some cases, as for the case study discussed in section 4, it was not possible to measure clear air upstream; instead, clear air measurements were made downstream in air at the appropriate θ_e. Next, below-cloud passes were conducted to obtain WCR and WCL measurements of cloud structure, followed by cloud-level passes both along and against the prevailing wind direction. When higher cloud passes were possible, additional sampling of air upstream or downstream of clouds was made to assess aerosol properties at different levels. These various data provided initialization conditions for the model simulations described in this paper.

3. Parcel model

The parcel model used in this study is an extended version of the Lagrangian adiabatic parcel model developed by Feingold and Heymsfield (1992). The original parcel model calculated droplet growth by condensation in an adiabatic updraft, or along trajectories, with prescribed atmospheric parameters. The changes to the original parcel model to allow for treatment of the ice phase are described in Eidhammer et al. (2009). Briefly, we included a routine to describe ice nucleation and crystal growth, modified the parameterization of water activity (the ratio between water vapor pressures of a solution and of pure water under the same conditions), and modeled hygroscopic growth of solution drops following Petters and Kreidenweis (2007).

The heterogeneous ice nucleation parameterization by PDA08 is based on selected field measurements and is constrained by laboratory measurements. Three

different types of aerosols are defined for the parameterization: dust–metallic compounds, black carbon, and insoluble organics, active in proportions that are based on measured chemical speciation of collected ice nuclei and on other assumptions used to fill knowledge gaps. The number of active IN ($n_{\mathrm{IN},X}$) from an aerosol population with these components X is given in PDA08:

$$n_{\mathrm{IN},X} = \int_{\log(0.1\mu m)}^{\infty} \{1 - \exp[-\mu_X(D_X, S_{i,v}, T)]\}$$
$$\times \frac{dn_X}{d\,\log D_X}\,d\,\log D_X, \tag{1}$$

where μ_X, the average activated IN per aerosol of size D_X, is defined as

$$\mu_X = \alpha_X H_X(S_{i,v}, T)\xi(T)\left[\frac{n_{\mathrm{IN},1}(S_{i,v}, T)}{\Omega_{X,1,*}}\right]\frac{d\Omega_X}{dn_X}. \tag{2}$$

Here T is the temperature and $S_{i,v}$ is the ice saturation ratio. The calculated IN concentration (as a function of T and $S_{i,v}$) is scaled to measured concentrations of IN smaller than 1 μm [$n_{\mathrm{IN},1}(S_{i,v}, T)$] and to the background aerosol surface area for particles with diameters between 0.1 and 1 μm ($\Omega_{X,1,*}$). The IN and aerosol measurements used for scaling were from the Ice Nuclei Spectroscopy (INSPECT) I and II field campaigns (DeMott et al. 2003; Richardson et al. 2007). However, after a reevaluation of the background aerosol surface area for dust–metallic compounds (DM) in PDA08, it was clear that the estimated surface area is only based on the INSPECT I data. Thus, for this study we chose to use an average aerosol surface area $\Omega_{\mathrm{DM},1,*}$ from the two INSPECT campaigns as the reference value (2.0×10^{-6} m^2 kg^{-1}, compared with 5.0×10^{-7} m^2 kg^{-1} as suggested in PDA08) since the IN concentration $n_{\mathrm{IN},1}(T, S_{i,v})$ is scaled to measurements from both INSPECT campaigns. We used the background aerosol surface values for black carbon and organic carbon as recommended in PDA08. The term $d\Omega_x/dn_x$ in Eq. (2) is the surface area for particles with diameters >0.1 μm, as calculated from the input size distributions for type X particles assumed for the simulations. The prefactor ξ allows droplets to freeze only below -2°C and is a cubic interpolation that goes from 0 to unity between -2° and -5°C. The factor H_X accounts for the fact that only a fraction of the available IN can function as deposition nuclei at water subsaturated conditions, depending on temperature. The term α_X is the fractional contribution from aerosol type

X to the measured IN concentration. Finally, the PDA08 parameterization was based mainly on CFDC data collected at relative humidities below water saturation where deposition nucleation dominates, but it includes a constant factor to enhance ice formation in the condensation and immersion freezing regime above water saturation. The equations for the individual terms in Eq. (2) and more detailed descriptions of this parameterization can be found in PDA08.

We also examined the suitability of a new ice nucleation parameterization described by D10 on the basis of ice nuclei and aerosol concentrations measured in multiple field projects. This parameterization represents immersion and condensation freezing and is a simple power-law function for IN number concentrations active under water supersaturated CFDC conditions:

$$n_{\mathrm{IN},T_K} = a(273.16 - T_K)^b (n_{\mathrm{aer},0.5})^{[c(273.16-T_K)+d]}, \qquad (3)$$

where $a = 0.000\ 059\ 4$, $b = 3.33$, $c = 0.0264$, and $d = 0.0033$; T_K is cloud temperature (K), $n_{\mathrm{aer},0.5}$ (cm^{-3} at STP) is the number concentration of aerosol particles larger than 0.5 μm, and n_{IN,T_K} is IN number concentration (L^{-1} at STP). The equation is strictly valid over the temperature range of data used, which was from $-10°$ to $-34°$C and at water supersaturation. While this simpler parameterization does not account for chemical speciation impacts on IN or multiple ice nucleation mechanisms, it describes the observed strong relationship between number concentrations of particles with diameters larger than 0.5 μm and IN number concentrations active in the water supersaturated cold cloud regime particularly relevant to mixed-phase clouds.

4. Case study results

a. Measurements

We focus here on a wave-cloud mission (RF04) on 18 November. During this flight, wave clouds in two areas were targeted. IN measurements were obtained in and around the second cloud region, located near the Wind River Range, Wyoming. Clear-air aerosol measurements in the region downwind of this cloud were obtained and were used as initial conditions for the model.

The cloud sampling levels were from 7000 to 7700 m above sea level (or 5300–6000 m above ground level) in the free troposphere. The temperature in the cloud and surrounding environment at these levels was between $-20°$ and $-30°$C, with the lower temperatures found in the cloud because of the nature of wave clouds (the air inside the cloud originates from a lower altitude than the

FIG. 1. Image from the forward camera on the C-130 aircraft on approach to the wave cloud at 2242:53 UTC. Approach is into the downstream edge of the cloud. Overlying but separate clouds are visible above the target cloud.

air at same level outside the cloud and has therefore cooled adiabatically when lifted). The horizontal wind was blowing from the west-northwest with a wind speed of close to 25 m s^{-1}. Back trajectories (48 h) suggest that the air mass originated from over the Pacific Ocean, entering continental regions over the southern Oregon coast and passing over southern Idaho before reaching the Wind River Range.

1) IN CLOUD

Figure 1 shows an image of the cloud that was targeted; Fig. 2 shows lidar and radar data for the same pass (at ~7250-m altitude) through the cloud. The wind direction is from right to left relative to the radar and lidar images. The main body of the cloud was about 600–700 m deep, while a cloud tail consisting of mainly ice crystals streamed downwind, the source altitude of which is unclear from the images. The horizontal extent of the cloud along the wind direction was up to 20 km. As seen in the cloud lidar images, there was also a cloud layer about 1000 m above the sampled cloud, but the two cloud layers seemed to be separated, at least in the entry regions of the cloud where seeding of ice into the lower sampled cloud was not likely. Figure 3a shows the measured updraft velocities and the number concentrations of cloud droplets, CVI cloud residuals, and out-of-cloud condensation nuclei (CN) from the same flight pass as the radar and lidar image. The measurements indicated that the targeted cloud was a wave cloud with a sinusoidal wave structure with vertical velocities between -3 and $+2$ m s^{-1} in this specific flight pass. Furthermore, comparison of cloud droplet with CN number concentrations with sizes >15 nm indicates near complete activation of aerosol particles >15 nm to cloud droplets in this case. Note, however, that the CN values are not necessarily those from the same air feeding the
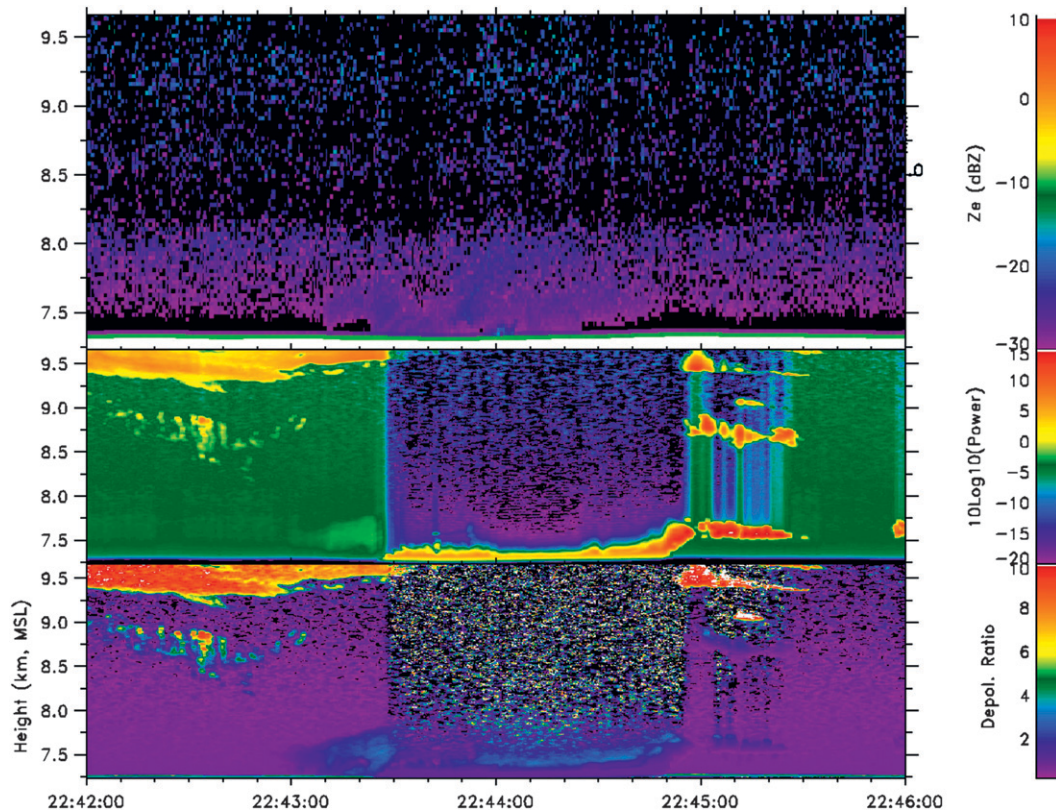
FIG. 2. (top) Radar reflectivities, (middle) lidar power, and (bottom) depolarization ratio above flight level 7250 m for the cloud pictured in Fig. 1. Wind direction is from right to left. Distinct and separate upper cloud layers are also noted in these data. Note that the enhanced radar signal in the background between 7.5 and 8 km is due to leakage of WCR transmitter to the receiver and does not originate from hydrometeors.

cloud, but they do approximate the layer values. CCN measurements with the Desert Research Institute airborne CCN spectrometer (Hudson 1989) during ICE-L confirm that high fractional activation occurred in many of the wave clouds because of the high water supersaturations driving droplet activation of most particles, and this was confirmed for RF04 (J. Hudson 2008, personal communication). The total CVI residual number concentrations (CVCNs) were about half of the cloud droplet number concentrations due to the CVI 50% cut size at 7-μm diameter. This was typical for many of these cloud passes. It is possible that IN number concentrations measured in this situation need to be corrected for this loss factor, but we assume that when processing residuals at the approximate cloud temperature in the CFDC, the source of IN is from the ice crystals alone and these are unlikely to be less than 7 μm for very long.

The IN number concentrations measured from CVI residual particles in the same wave pass at 7250 m are shown at 1 Hz (values reflect digital counts from 1 to 3 s^{-1}, and zero otherwise) and with a 30-s running mean applied in Fig. 3b, along with residual 1-Hz particle number concentrations at sizes larger than 0.5 μm from the CFDC optical particle counter. These data show that IN are measured only within the body of the cloud, as expected when sampling via the CVI, and that application of a running average value suggests correlation of IN number concentrations with those of aerosol particles larger than 0.5 μm in the sense indicated by D10. Nevertheless, considering the sampling statistics of the extremely low IN number concentrations determined, we will report the IN number concentrations as an average for each cloud pass for comparison to ice crystal number concentrations.

There were a total of seven flight passes directly below or through the cloud, at different altitudes. The passes were parallel to the horizontal component of the wind and occurred at altitudes between 6950 and 7700 m and temperatures between $-23°$ and $-30°$C as seen in Fig. 4, where the gray shaded areas indicate the cloud passes.

The tracks of each individual cloud pass as functions of longitude and latitude are shown in Fig. 5a, where the numbers indicate the sequence of the passes. Black lines indicate a west–east passage (along wind) and gray lines
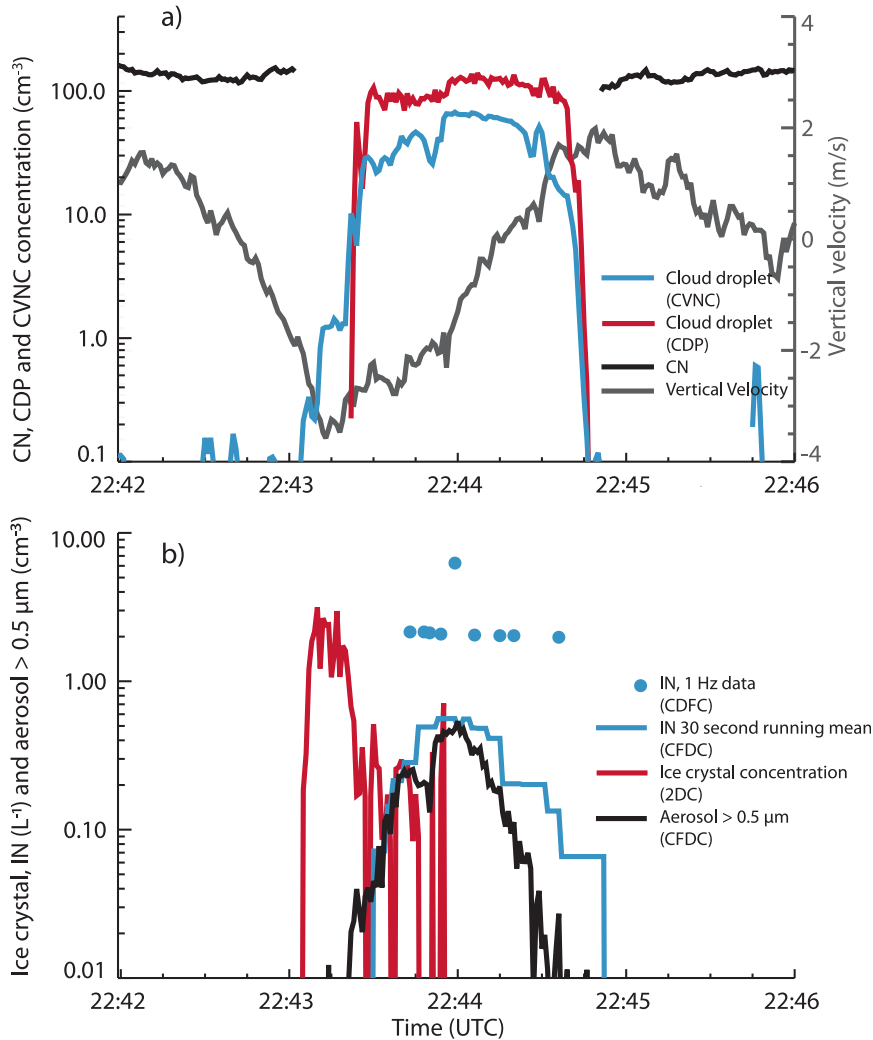
FIG. 3. Data from the cloud pass depicted in Figs. 1 and 2, executed from downstream (left side of figure) to upstream across a wave. (a) Condensation nuclei (CN; black curve), cloud droplet concentration (CDP; red curve), and CVI cloud droplet and ice residual nuclei (CVCN; blue curve) number concentrations are shown on the left axis, while vertical motion (gray curve) is shown on the right axis. CN values are omitted in the region of liquid and ice cloud particles since data are potentially subject to sample inlet artifacts there. CVCN number concentrations are about ½ of CDP number concentrations, consistent with the 50% CVI cut size of 7 μm and the observed cloud droplet size distribution. (b) Ice crystals (red curve), 1-Hz IN (blue dots), and 30-s running mean IN (blue curve) concentrations. The black curve is the 1-Hz concentration of cloud residual aerosols >0.5 μm.

indicate an east–west passage (against the prevailing flow). Also shown is the track of the aircraft downwind of the cloud area at the θ_e corresponding to the cloud pass (dashed line). Altitude levels are indicated in Fig. 5b.

Figure 6 shows measured vertical velocities and number concentrations of ice crystals, droplets, and average IN (ice crystal residuals sampled behind the CVI that acted as IN) concentrations in the entire pass, for each individual cloud pass as a function of time. Average ice crystal concentrations are also shown for comparison

with average IN concentrations. The plots are ordered according to the altitude of the aircraft. For example, passes number 3 and 7 were at the same altitude (and almost at the same horizontal coordinates) but 35 min apart. Gray shaded areas indicate the cloud, with the width of the cloud in meters shown, and arrows illustrate the airflow relative to the flight direction. In using the concentrations of particles >63 μm measured with the NCAR 2D-C probe to define ice crystal concentrations, we assumed that newly formed ice crystals grew rapidly
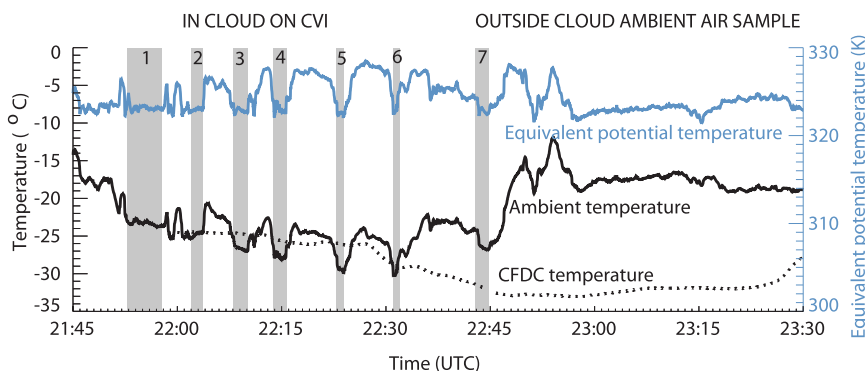
FIG. 4. Measured ambient (black solid curve) and equivalent potential temperature (blue curve). Also shown are CFDC processing temperature (dotted curve). Gray areas indicate cloud passes.

in the ice supersaturated conditions. Also, there are large uncertainties in the determination of sample volume in the 2D-C probe associated with smaller sizes. The rapid growth of ice crystals is supported by diffusional growth calculations [see, e.g., Figs. 13–34 in Pruppacher and Klett (1997)], which show that growth to about 60 μm occurs in close to 2 min for a variety of habits and temperatures at water saturation. A 2-min trajectory transit time in the cloud corresponds to about a 20-s C-130 transit time and is about $\frac{1}{5}$ of the trajectory time in the cloud. Further, the choice of 63 μm minimized contamination of the ice crystal measurements from large cloud droplets that might fill one or two single pixels of the imaging volume, but it limited our ability to pinpoint the exact point of ice initiation by the detection of smaller ice crystals. We might also have missed some evaporating small ice crystals in the tail of the cloud. The 2D-C data showed that ice crystal concentrations were

between ~0.1 and 3 L^{-1} (black curve), with the highest concentration in the last pass.

Except for pass 7, CFDC measurements were conducted at processing temperatures close to the ambient temperature (black curve in Fig. 4). The warmer temperatures in the CFDC of up to 3°C in some of the passes compared to the environment are not expected to affect the measured IN concentrations significantly compared to if they were measured at the same temperature as the environment for the same aerosol conditions (PDA08; D10). The average measured IN concentrations from cloud residual particles were up to 0.2 L^{-1} (yellow line in Fig. 6) and were generally in good agreement with the average 2D-C probe measurements (blue line). The values for the average IN and ice crystal concentrations are shown in Table 1, along with the average CFDC processing temperature and supersaturation in each pass. These extremely low IN concentrations would be
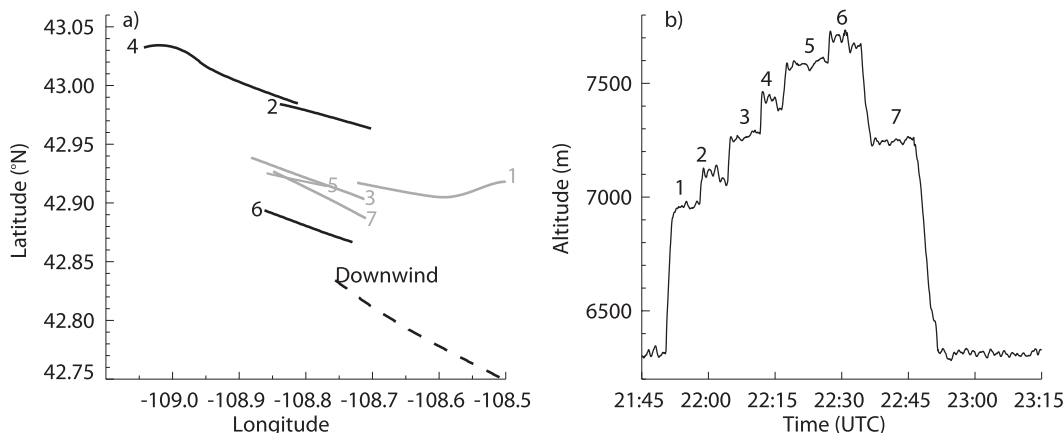

FIG. 5. (a) Flight tracks of each cloud pass. Numbers show the sequence of cloud passes. Black lines indicate a west–east passage and gray lines indicate an east–west passage. Dashed line indicates the location and direction of the path of the aircraft downstream of cloud following pass 7, with an end point at 42.2°N, 106.8°W in the time period 2258–2315 UTC. (b) Altitude of the aircraft through the cloud passes.
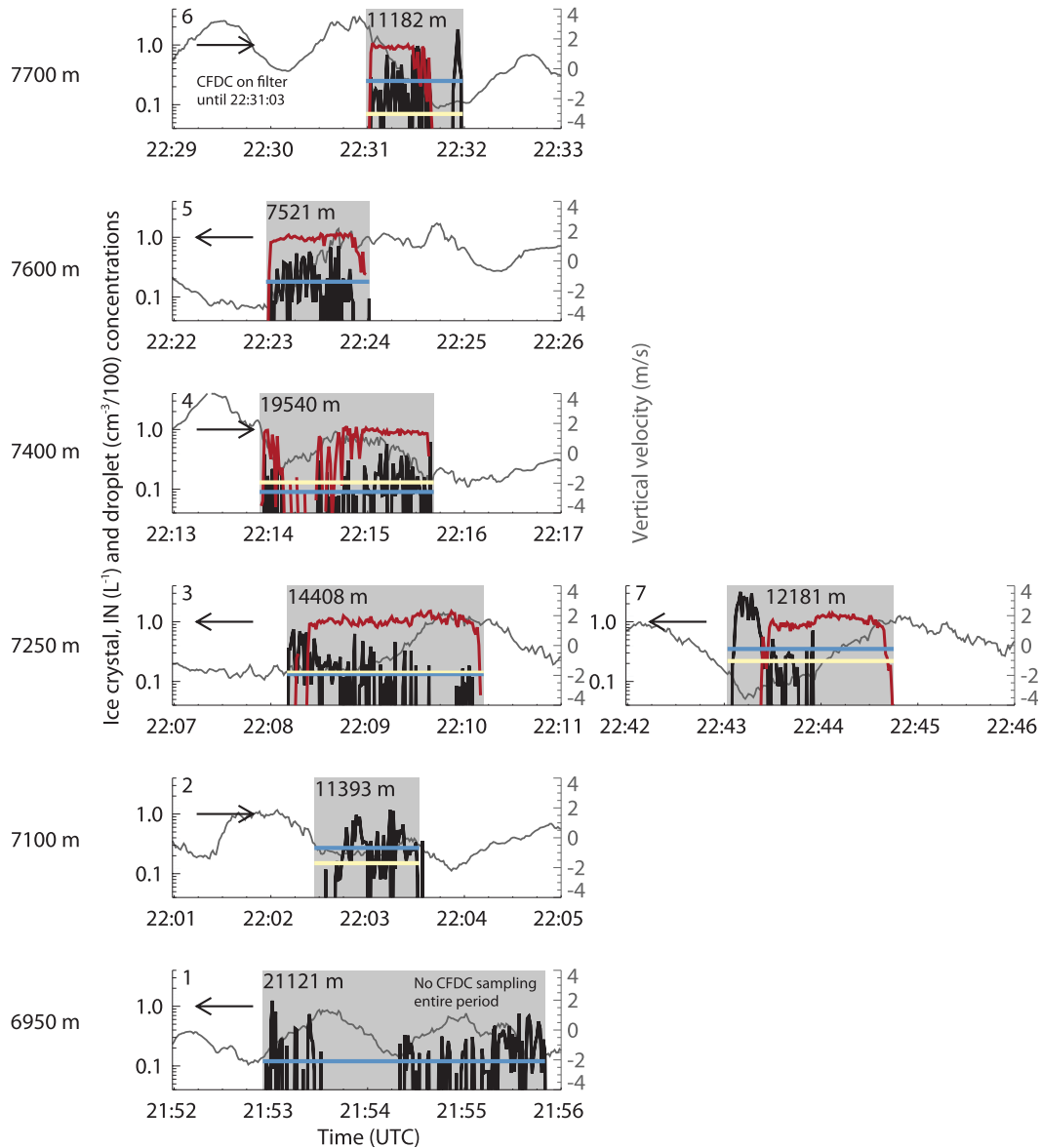
FIG. 6. Average IN (L^{-1}; yellow), ice crystal (L^{-1}; black), average ice crystal (L^{-1}; blue), and droplet concentration [cm^{-3} (100)$^{-1}$; red] as a function of time for the seven different cloud passes. Each pass is plotted as a function of altitude. Numbers in the upper left corner corresponds to the flight pass number as shown in Fig. 5. The values in the gray shaded area indicate the extent of the cloud pass in meters. Gray lines show the measured vertical velocities (m s^{-1}). Arrows indicate the direction of the airflow relative to the flight track (pointing toward right for flight track along the airflow).

difficult to measure with any confidence without the enhancement of number concentrations provided by the CVI inlet, which lowers the detection limit for ice nuclei by the CFDC method to around 0.01 L^{-1} (D10). During passes 2 and 3 the CFDC was processing residuals at conditions 5% subsaturated with respect to water (see Table 1). Interestingly, this did not have a major impact on IN number concentrations compared to passes in which processing was done in the

supersaturated regime favoring condensation and immersion freezing. This suggests that deposition nucleation or immersion freezing of haze particles is occurring very close to water saturation for these cloud conditions. During pass 1 the CFDC was not yet sampling from the CVI; thus, no IN could be detected. At the top of the cloud, in passes 5 and 6 the IN concentrations are very low because of the short time period within the cloud (made shorter by the sample filter being on for the

TABLE 1. Average CFDC processing temperature and supersaturation and average IN and ice crystal concentrations (from 2D-C) in the seven cloud passes.

Pass	CFDC temperature (°C)	CFDC supersaturation (%)	Average IN concentration (L^{-1})	Average ice crystal concentration (L^{-1})
1	No sampling	No sampling	No sampling	0.12
2	−24.5	−5	0.15	0.27
3	−24.9	−5	0.14	0.13
4	−25.7	1	0.13	0.09
5	−26.2	3	0.02	0.18
6	−29.1	1	0.07	0.25
7	−32.0	3	0.22	0.35

first 12 s of cloud in pass 6) and low counting statistics. Taking these various factors and uncertainties into consideration, we conclude that the general agreement between IN and ice crystal number concentrations indicates that ice formation was primarily via heterogeneous ice nucleation processes, with the possible exceptions noted below.

Pass 7 (Figs. 6 and 3b) was a special case for which the CFDC temperature was purposely lowered 5°C below the cloud temperature and the processing relative humidity with respect to water was set to 103% to measure temperature dependence within the immersion freezing regime and to loosely constrain potential contact freezing number concentrations on the basis of the ideas of Durant and Shaw (2005). IN number concentrations averaged for this cloud pass were the highest of the group of passes, and running average concentrations (Fig. 3b) peaked around 0.5 L^{-1}, similar to peak ice crystal number concentrations within the mixed-phase region of this cloud pass. IN lead the ice signal somewhat in time, likely because of the need for ice crystals to grow to sizes of 63 μm prior to clear detection as ice. Overall, the results suggest relatively weak IN temperature dependence over a 5°C interval and thus no unusually strong source for contact freezing nuclei in evaporating regions of cloud.

The cloud was mixed-phased in most of the regions sampled, with cloud droplet concentrations between 100 and 150 cm^{-3} (red curve in Fig. 6, divided by 100). A few parts of the cloud consisted of ice-only tails, such as in the entire first and second passes. This is verified by the lack of measured cloud droplets with the CDP and no detection of supercooled liquid by the RICE probe (not shown here). These passes were through portions of the cloud that had descended from higher altitudes and lower temperatures. The cloud radar and lidar data (Fig. 7) showed that both of the first two passes were below the main body of the cloud. The parts of the cloud downwind of the liquid water cloud in passes 3 and 7 (7250 m) were also composed only of ice, based on CDP (no drops present) and 2D-C measurements. The downstream ice

region for pass 7 is also evident in the lidar data of Fig. 2. At levels 7250, 7400, and 7600, droplets dominated over very small or immeasurable numbers of ice crystals in the upstream entry region of the cloud, suggesting that ice is formed very close to the leading liquid cloud edge via condensation or immersion freezing after droplets are formed, or by deposition nucleation only very close to the leading edge. Lidar data support the same conclusion. If ice is formed by deposition at, for example, 95% relative humidity with respect to water, the ice would form about 5 s before the C-130 entered the mixed phase part of the cloud. However, ice has to grow to 63 μm before being detected by the 2D-C, making it difficult to distinguish the exact mode of freezing mechanism. This result and the generally modest increase of ice numbers with time and distance along a cloud pass, consistent with growth times for crystals to detectable sizes, reaffirms the conclusions that Cooper and Vali (1981) inferred from orographic cap clouds. There was no evidence for greatly enhanced ice nucleation in the wave cloud evaporation (downstream exit) zone in this case, as inferred in some other wave cloud studies (Cotton and Field 2002). Nevertheless, the downstream region of this cloud showed the presence of ice crystal concentrations up to 3 L^{-1} (Figs. 3b and 6, pass 7). No heterogeneous ice nucleation signature (for processing at −32°C) was associated with the few CVI inlet residual particles collected in this ice tail (Fig. 3b). This result contrasts with detection of ice nuclei in the ice tail penetrated at 7100 m in pass 2. Examination of the radar and lidar images for all passes suggests that the cloud top at times reached up to 8.4 km. Since a minimum cloud temperature of −30°C was detected at 7700 m in pass 6, the possibility that some parcels achieved conditions for homogeneous freezing (below −36°C) and impacted the lower cloud layers sampled cannot be ruled out. This is especially the case for the ice tail during pass 7, when cloud top was likely to have been above 8 km based on the remote sensing data.

The measured liquid water content (LWC) obtained from the King probe for cloud droplets from the CVI and integrated from the CDP size distributions is shown
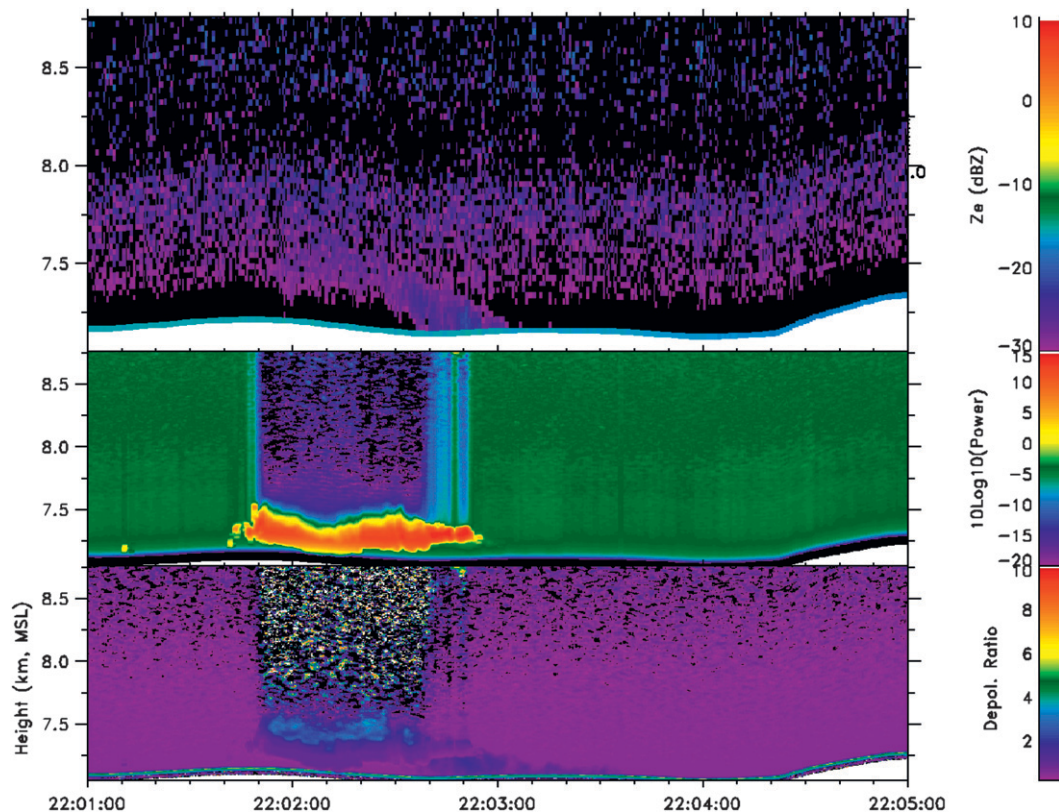
FIG. 7. As in Fig. 2, but for the second pass, showing the aircraft interception of the ice tail of the wave cloud below liquid cloud altitudes.

in Fig. 8 at different heights, as in Fig. 6. The LWC determined with the CVI was about half of the LWC measured directly by the King probe and the LWC integrated from the CDP, an expected result based on the 50% CVI cut size of 7-μm diameter and the observed cloud droplet size distributions.

Several other studies of wave and orographic clouds exist in the literature (Cooper and Vali 1981; Heymsfield and Miloshevich 1993; Field et al. 2001; Baker and Lawson 2006). The wave cloud studied here compares with other measurements at similar temperatures in many aspects. However, the ice crystal concentration observed for this cloud was very low, in closest accord with the results of Heymsfield and Miloshevich (1993) for clouds in the same geographic region and in a similar temperature regime. Cooper and Vali (1981) report ice crystal concentrations up to 200 L^{-1} at $-23°$C; Field et al. (2001) reported ice crystal concentrations of $\sim$10 cm^{-3}. Both these studies discuss the discrepancy between historical IN concentration and measured ice crystal concentration but conclude that some type of heterogeneous nucleation was most likely responsible for ice crystal formation. Nevertheless, ice nuclei measurements were not available for any of these other studies, nor were

radar and lidar data available to reveal the sometimes-complex structure of these clouds (Baker and Lawson 2006) and to give better inference to the potential source regions for ice. Both studies also represent high outlier observations compared to the compilation of Cooper (1986) of ice crystal concentrations present in assorted cloud types from multiple global locations for conditions that should not have permitted the influence of homogeneous freezing or secondary ice formation processes. In the present study we show that IN and ice crystal concentration compare reasonably well on the basis of reprocessing cloud residual particles in the case examined. While a full compilation of ice crystal concentrations in all ICE-L wave cloud cases is not yet published, Twohy et al. (2010) note similarly low ice crystal number concentrations ($\sim$1–5 L^{-1} for a range of temperatures down to $-30°$C) during five wave cloud flights during ICE-L when the influence of ice falling from colder temperatures was excluded.

2) OUT OF CLOUD

Aerosol and IN measurements in clear air were obtained downwind of the cloud (Fig. 9) at the same equivalent potential temperature as the in-cloud measurements
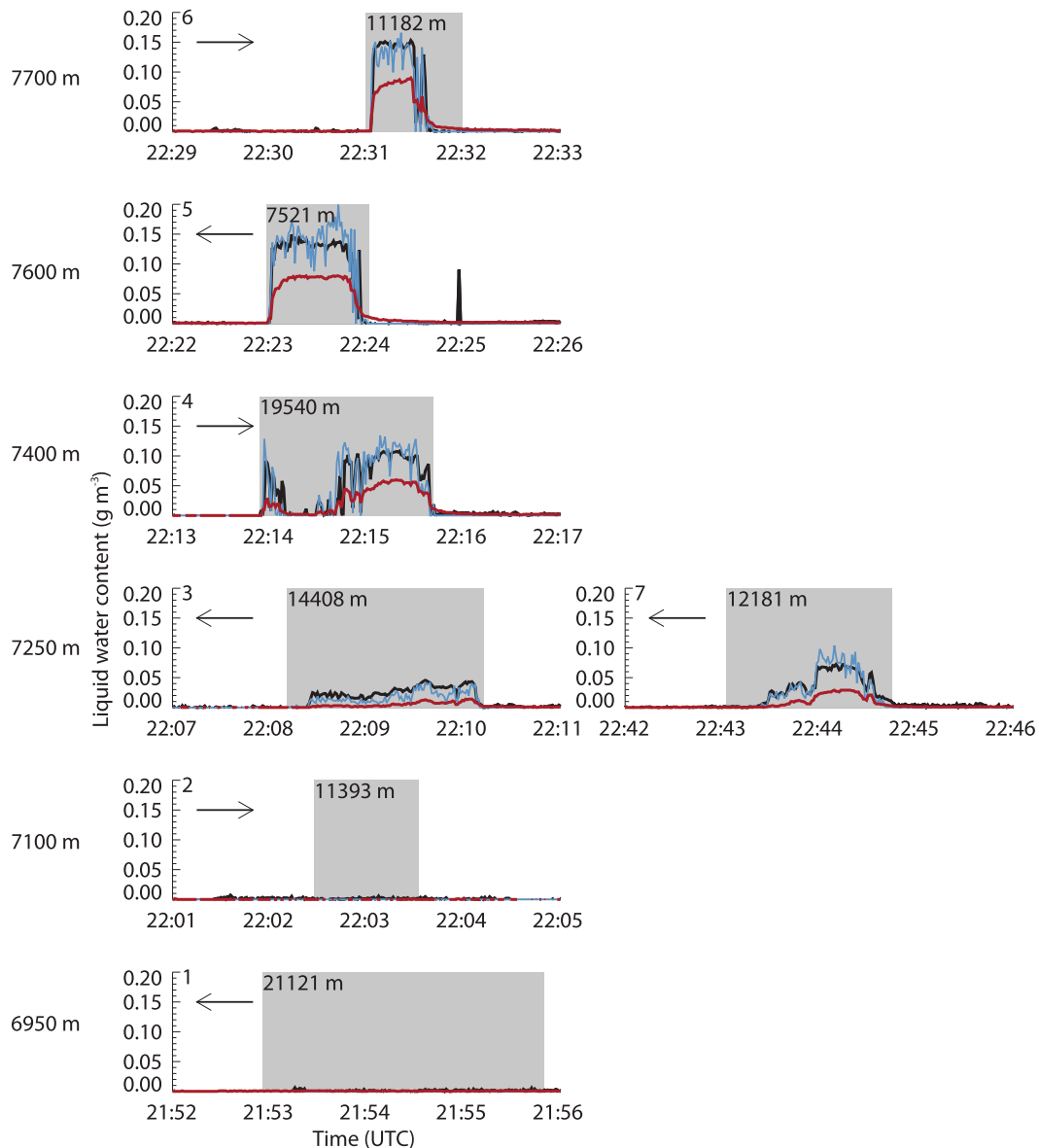
FIG. 8. As in Fig. 6, but for LWC. Blue lines are LWC integrated from size distributions reported by the CDP, black lines are LWC measured with the PMS King probe, and red lines are LWC from the CVI.

($\sim$322 K, blue curve in Fig. 4, after 2245 UTC). In Fig. 9 the gray areas indicate CFDC sampling periods while the white areas indicate CFDC filter periods used to determine background counts in the CFDC (Prenni et al. 2009). Average IN concentrations were determined for the intervals between the filter periods (filled triangles) and ranged from 0.05 to 1 L^{-1}. We note that the lowest values are below the approximate lower CFDC detection limit during standard (non-CVI) sampling ($\sim$0.3 L^{-1} for 1 L min^{-1} sampling) considering Poisson sampling statistics (D10). The maximum IN concentration was slightly higher than that for the in-cloud measurements,

but a slightly higher concentration was expected since the processing temperature in the CFDC was set lower than in-cloud temperatures to assess potential contact-freezing nuclei concentrations, as described in section 2. Overall the IN concentrations compared well for the two different inlet sampling configurations. Error bars for the IN measurements represent the 90% confidence interval of mean IN concentrations. The UHSAS number concentrations of particles >0.5 μm in diameter (black lines) are also shown since IN concentrations have been shown to positively correlate with particle number concentrations in this size range (Richardson et al. 2007;
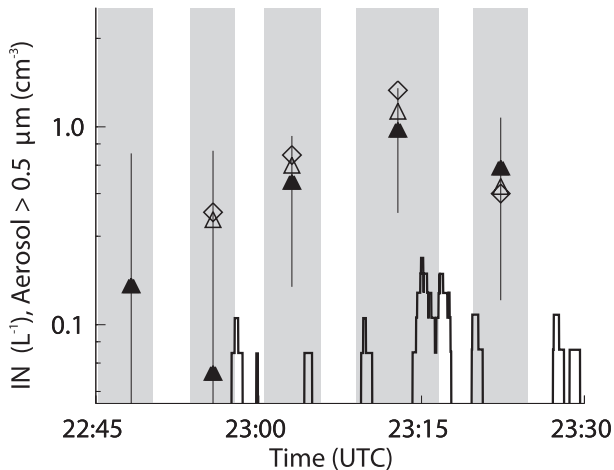
FIG. 9. Measured interval-averaged IN concentrations from the ambient air sample inlet (filled triangles). The lines through the filled triangles indicate the 90% confidence interval of the mean IN concentration. Gray areas here are measurement periods and white areas are CFDC filter periods. Black bars are aerosol concentration for particles >0.5 μm in diameter. Also shown are predicted IN concentrations using the PDA08 parameterization, but with a lower reference aerosol surface area ($\Omega_{DM,1.0,*}$) than recommended in the PDA08 paper (open triangles), and predicted IN concentration using D10 (open diamonds).

D10) and because this parameter serves as an input to the parameterization of D10. The highest IN number concentrations did indeed correspond to the highest aerosol concentrations, as shown in Fig. 9.

b. Parcel model initialization

The cloud focused on here was a long-lived stationary wave cloud. The vertical wind measurements in Fig. 6 indicate a sinusoidal wave structures and we assumed that mixing of parcels from different streamlines was negligible. Furthermore, for the relatively short transit time through the mixed-phase cloud, ice crystals did not have time to grow sufficiently for sedimentation to be significant. For example, the 2D-C measurements showed that the largest ice crystals were about 300 μm in diameter (with a mode of 150 μm) and, depending on shape, could be assumed to have fall velocities of up to 40 cm s^{-1} (Pruppacher and Klett 1997), much lower than the updrafts and downdrafts in the wave cloud (up to 3 m s^{-1}). Therefore, simple parcel model studies to investigate ice crystal formation in this cloud were suitable. For simplicity, we fit the trajectories of the parcels to a clean sinusoidal wave structure of ±2.3 m s^{-1}, which is close to the maximum value measured in several of the passes. We used a combination of measured potential temperature and the vertical wind component to estimate the wavelength of the sinusoidal as 2.3 km. With an average horizontal wind speed of 23 m s^{-1}, the wave parcel

transit time of one wavelength was about 16 min. The in-cloud transit time where ice was present was slightly less than the wave transit time, since the parcel was not in the ice supersaturated zone over this entire region. We ran three simulations with trajectories starting with different initial conditions (altitude, temperature, and mixing ratio). The initial temperatures and mixing ratios for the trajectories were taken from measurements downwind of the cloud as the C-130 aircraft ascended to complete the first pass in the cloud (2150:30–2152:10 UTC). Figure 10 shows the measured temperatures and vapor mixing ratios along with the assumed initial conditions (black dots). Measurements were only obtained from altitudes of 6300 m and higher in the vicinity of the cloud; therefore and we cannot include trajectories closer to or at cloud base.

For aerosol input parameters, we used fitted size distributions from UHSAS and CN measurements from 2258 to 2312 UTC downwind of the cloud, where the equivalent potential temperature was ~323 K. Note that because of noise in the first nine channels in the UHSAS, we limit sizes to >0.1 μm. For our simulations, we assumed that the aerosols upwind and downwind were the same; we cannot assess the possible impact of chemical cloud processing on the aerosols. The input temperature and humidity profiles are from different time periods than the aerosol distributions. The profiles were obtained over a short time period where a vertical profile could be obtained, while the aerosol distribution was obtained for a longer time period to reduce counting errors in the aerosol measurements.

For a second type of comparison we calculated predicted IN concentrations from the two parameterizations described above, using four different input aerosol distributions, taken from the same time periods when the CFDC was sampling ambient air. These predicted IN concentrations were calculated (i.e., static IN prediction) for the same temperature and saturation conditions as the CFDC measurements and were compared with the measured IN number concentrations.

The 14-min average UHSAS aerosol distribution used for the modeling study is shown in Fig. 11, along with a fit to the data using three lognormal modes. Since the PDA08 parameterization bases predicted IN on aerosol surface area, both number and surface aerosol distribution are shown in Fig. 11. Clearly the measured concentrations of coarse-mode particles were low, and the uncertainties in the fitted distributions are large [Poisson sampling errors (Snider and Petters 2008) are between ±0.2–0.4 cm^{-3} for particles >0.5 μm]. Further, the sizes measured with UHSAS were limited to >0.1 μm. However, CN measurements immediately downwind of the cloud showed a concentration of ~150 cm^{-3} (see
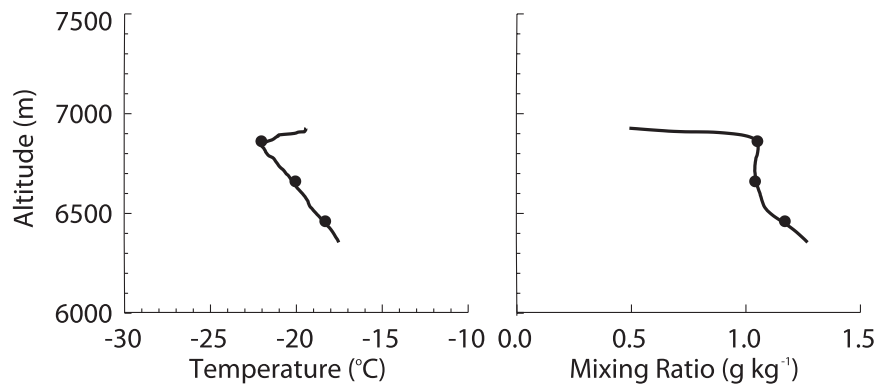
FIG. 10. Measured temperature and vapor mixing ratio from the time period 2150:30–2152:10 UTC (solid line). Black dots indicate the initial conditions for the three model trajectories.

Fig. 3), and this total number concentration was used to constrain the size distribution fit, particularly the magnitude of smallest mode, which contained most of the number concentration.

The D10 parameterization for IN requires the number concentrations of particles with diameters >0.5 μm, which were readily determined by integrating the contributions from each of the three fit modes. However, the PDA08 parameterization requires not only surface area but also information about the particle type. Further, the activation of particles into liquid cloud drops, which is calculated independent of PDA08 or D10, also depends on their chemical composition. We used aerosol composition measurements during clear-air and cloudy periods around the time of the cloud passes to constrain assumptions required for simulating liquid and ice cloud formation. The C-ToF-AMS indicated a sulfate-dominated (approximately $\frac{2}{3}$ sulfate and $\frac{1}{3}$ organic by mass) aerosol with a broad sulfate mass distribution centered at a vacuum aerodynamic diameter of 0.25 μm, corresponding to a mass mode aerodynamic diameter of 0.18 μm. This mode diameter is between the mass mode diameters of our first two fitted lognormal modes. In addition, the liquid-phase cloud residual particles below
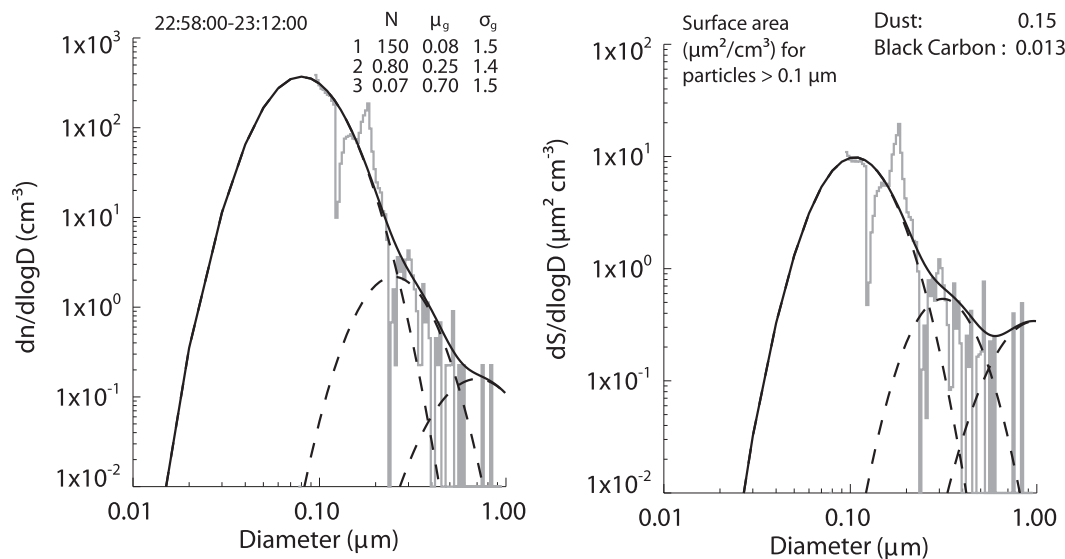

FIG. 11. Measured 14-min average aerosol distributions (gray bars) and fitted size distributions for the time period 2258–2312 UTC. Individual distributions are shown with dashes and total distribution is shown with solid lines; (left) size distribution; (right) surface area distribution. Legends in the left-hand plot give the values for the fitted distributions [number concentration (N, cm^{-3}), mean diameter (μ, μm), and geometric standard deviation (σ)]. Since the PDA08 parameterization is dependent on surface area for particles >0.1 μm, legends in the right-hand plot give these values. Black carbon surface area is calculated from distribution 1, assuming a number concentration of 0.5% out of the total numbers. Dust surface area is calculated from distribution 3.

about 0.4 μm were dominated (>70% by number) by sulfate compositions, as indicated by Transmission Electron Microscopy (TEM) analyses. We therefore assume that both the first (smallest) and second modes were composed mainly of ammonium sulfate, and a hygroscopicity parameter $\kappa_{as} = 0.6$ (Petters and Kreidenweis 2007) was used to compute cloud droplet activation. Black carbon measurements from the SP-2 indicated a number size distribution centered at a mass-equivalent diameter 0.08 μm, with nearly the same dispersion as the fitted first mode. Measured black carbon number concentrations represented approximately 0.5% of the particles in this fitted mode, and we assumed they were distributed by size according to the fitted mode-1 parameters [in Fig. 11 this corresponds to a number concentration of 0.75 cm^{-3}, and a surface area of black carbon >0.1 μm (available for freezing in PDA08) of 0.013 μm^2 cm^{-3}]. These black carbon particles were allowed to serve as both CCN ($\kappa_s = 0$) (Dusek et al. 2006) and IN in the PDA08 parameterization. ATOFMS measurements and TEM single particle analyses indicated that most (70% or more by number) of the particles with diameters larger than 0.4 μm were composed of Na-K-Mg-Ca-Cl, sometimes mixed with sulfate, nitrate, and/or small amounts of silicates; these compositions are representative of dry lakebed playa salt dust (Pratt et al. 2010). Therefore, the largest mode was assumed to have $\kappa_d = 0.7$ as measured for dry lakebed dust from the western United States (Koehler et al. 2007). Several percent of the particles with diameters >0.4 μm were dominated by silicates. Both the playa and silicate dust particle types in mode 3 were assigned to the PDA08 dust IN category because of the presence of silicates in some fraction of typical playa dust particles. Koehler et al. (2007) observed heterogeneous ice nucleation from 1 in 100 playa dust particles (including some silicates) at −35°C and for sizes up to 0.4 μm. Ice formation for smaller active fractions is plausible for larger playa dust particles at the warmer cloud temperatures in this case.

c. IN and ice crystal prediction results

1) DYNAMIC CLOUD MODEL

Figure 12 shows modeling results for the three different parcel trajectories using both the PDA08 and D10 parameterizations. The outputs from each trajectory are shown with a different grayscale. The ice crystal concentration was predicted to be up to 0.3 L^{-1} (about ¾ of them from the dust and ¼ from the soot distribution) with the PDA08 parameterization and 0.5 L^{-1} with the D10 parameterization. These predicted values were in good agreement (within about a factor of 3) with the range of measured IN and ice crystal concentrations (see

Fig. 6 and Table 1). The predicted ice crystal concentrations were highest in the upper trajectory, where the lowest temperatures were reached.

The maximum mean ice crystal size was 150 μm, which compares well with the median size distribution from the 2D-C measurements (not shown here). The maximum supersaturation with respect to water in the trajectories was between 0.6% (lowest trajectory) and 1.3% (highest trajectory), enough to activate almost the entire aerosol population (i.e., all particles with diameters >0.25 μm) into cloud droplets (~150 cm^{-3}). The predicted cloud droplet concentrations were slightly higher than measured values, indicating either that the aerosol concentration used as input was also slightly higher than the real one or that there were greater numbers of smaller and/or less hygroscopic particles than assumed.

The maximum modeled liquid water content was between 0.02 and 0.09 g m^{-3}, with the larger values associated with the upper trajectories. This LWC was less than the maximum measured LWC (Fig. 8), which showed measured LWC of ~0.15 g m^{-3} at the top of the cloud.

In the downwind part of the cloud, the droplets evaporated immediately (<1 s) after reaching a relative humidity with respect to water of 98%. The ice crystals, however, were too large to completely evaporate in the wave valley where the relative humidity with respect to ice was less than 100%, and an ice tail was simulated. The lidar measurements detected an ice layer that extended down to about 6700 m, supporting the existence of an ice tail (see Fig. 7).

Since the maximum vertical velocity in pass 6 was close to 3 m s^{-1}, there were some variations in the vertical velocities in the cloud. We therefore also conducted simulations assuming vertical velocities of 3 m s^{-1} to see the bounds of what to expect. In these simulations, the temperature reached about 2°C lower than in the simulations with 2.3 m s^{-1}. This allowed for an increase in ice crystal concentration of ~(0.03–0.53) L^{-1} with D10 and to 0.42 L^{-1} with PDA08. Further, the liquid water content also compares better with measured LWC. This suggests that localized variations in the updraft velocity in the different passes can explain the discrepancy between modeled and measured LWC in the 2.3 m s^{-1} simulations.

2) STATIC ICE NUCLEI PREDICTIONS

In the previous section, we used an average aerosol size distribution to compare modeled with measured in-cloud parameters, assuming an idealized wave structure. In this section we compare predicted IN concentrations from the PDA08 and D10 parameterizations with IN measurements downwind of the cloud (static predictions).
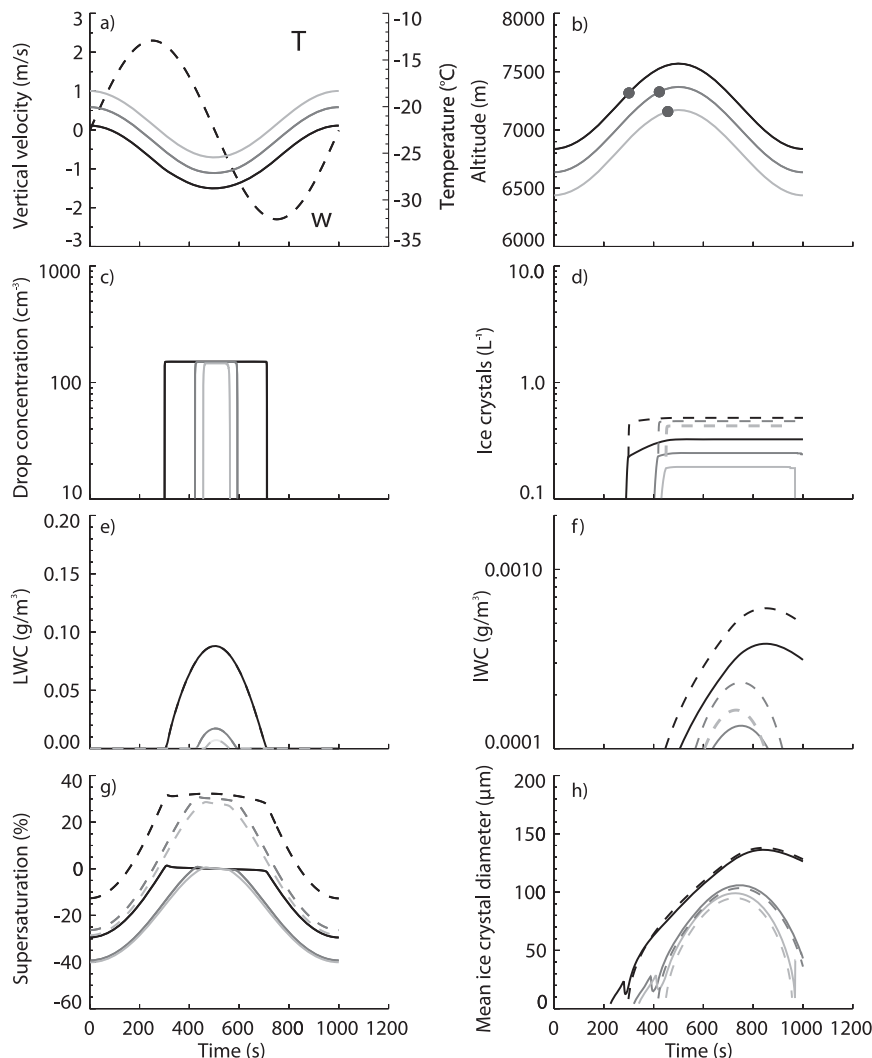
FIG. 12. Modeling result in an idealized wave cloud along trajectories. (a) Vertical velocity (dashed line) and temperature (solid line). Each trajectory is indicated with different shade of gray. (b) Trajectory altitude and lifted condensation level (circle), (c) droplet concentration, (d) ice crystal concentration (solid curves with PDA08 and dashed curves with D10), (e) LWC, (f) ice water content, (g) supersaturation over water (solid line) and ice (dashed line), and (h) mean ice crystal diameter.

As inputs to the parameterizations, we used the measured size distributions from the same time periods as the CFDC sampling time periods (Fig. 13), with similar assumptions about composition as discussed for the wave cloud case study above, and applied the same temperature and supersaturation conditions as in the CFDC. The results are shown in Fig. 9 as open triangles (PDA08) and open diamonds (D10). Generally, the predicted ice crystal concentrations from PDA08 were in very good agreement with the IN measurements using our corrected value for the background aerosol surface area of dust ($\Omega_{DM,1,*}$) after reevaluation of the INSPECT data. The predicted concentration would increase by a

factor of 4 if the suggested value given in PDA08 were used. The D10 parameterization predicted slightly higher IN concentrations on average but was still in very good agreement with measurements. The concentrations of coarse-mode particles were low, and the statistics in the individual size distributions in Fig. 13 have large uncertainties (Poisson sampling errors are between ±0.4–0.7 cm^{-3} for particles >0.5 μm). Nevertheless, the measured IN concentrations for each sample period followed the same trends as seen for measured and modeled IN concentrations, responding to changes in number concentrations of particles larger than 0.5 μm and to surface area concentrations of particles larger than 0.1 μm.
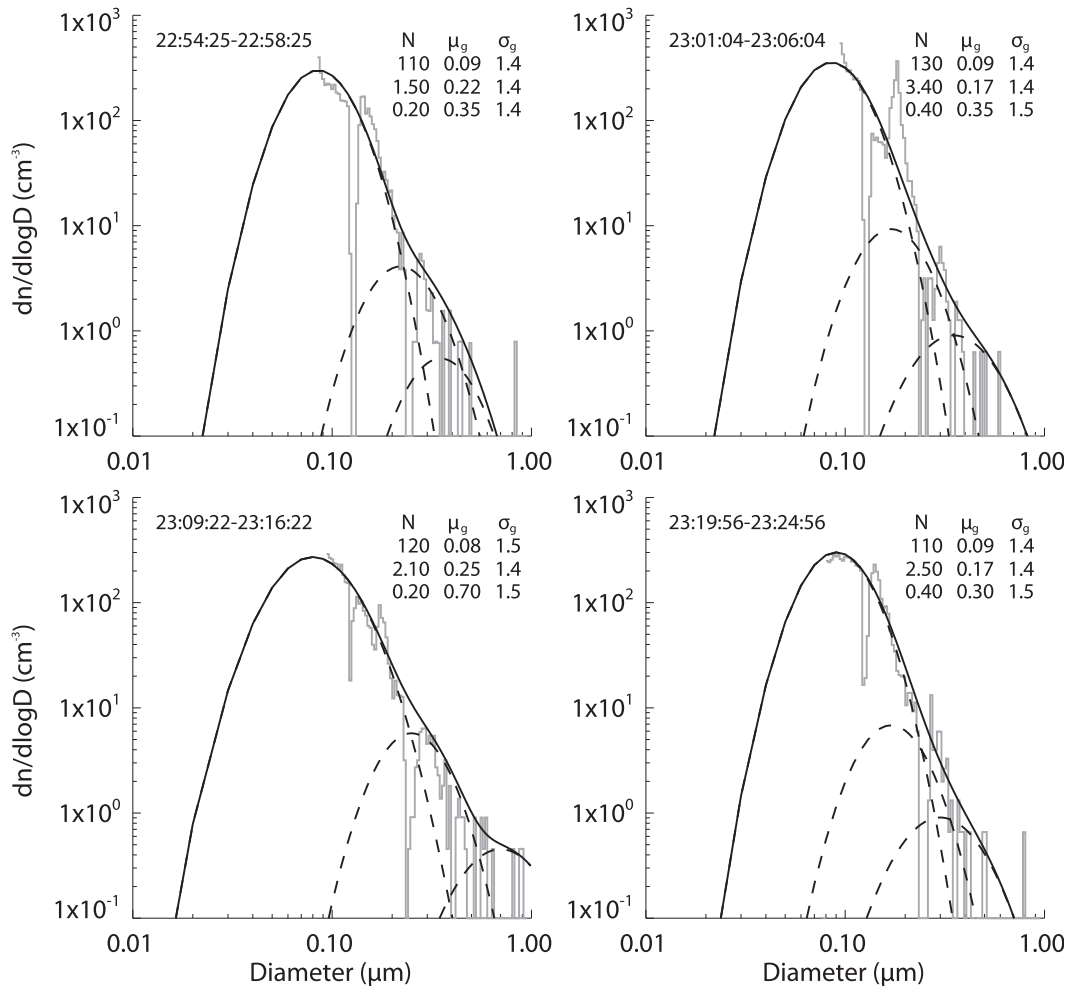
FIG. 13. UHSAS-measured aerosol size distributions (gray bars) and fitted size distributions (lines) for the time periods of CFDC measurements. Individual distributions are shown with dashed lines; total distributions are shown with the solid line.

5. Discussion and conclusions

In situ measurements of IN, ice crystal, and aerosol concentrations were obtained in and downwind of a wave cloud. The observed cloud was a long-lived stationary wave cloud, with a nearly sinusoidal wave structure. The measurements here show for the first time that IN measured both from cloud residual particles and from air entering a series of wave clouds compare well in number with ice crystals observed to nucleate in the same clouds. These results differ from conclusions of some previous studies (Cooper and Vali 1981; Field et al. 2001; Baker and Lawson 2006), where ice crystal concentration measurements were deemed not to be in accord with expectations from historical ice nuclei measurements. The clouds in the present case were of a nearly ideal nature for comparisons, while

complexities and depth of cloud layers in the Baker and Lawson (2006) studies may have masked the roles of known primary nucleation versus homogeneous freezing or other unknown mechanisms that were not clearly evident during ICE-L. The critical availability of airborne radar and lidar data in the present study also points out the possibility that clouds in some previous work may have been unknowingly influenced by seeding from lower temperatures where homogeneous freezing occurs. Finally, instrument artifacts, such as shattering of ice crystals on the inlet probes (Field et al. 2003; McFarquhar et al. 2007; Jensen et al. 2009), are also a potential cause for apparent discrepancies in some previous studies. Since the ambient temperature was above the $\sim -36°C$ temperature required for homogeneous freezing, and the measured IN and ice crystal number concentrations were in close agreement, heterogeneous ice

nucleation mechanisms were most likely responsible for ice formation in this cloud. Ice crystals were detected only after the formation of cloud droplets. The strong forcing and high supersaturations in the cloud led to near-complete activation of aerosols to droplets, suggesting likely ice nucleation mechanisms leading to condensation and immersion freezing, and possibly contact freezing inside out (Durant and Shaw 2005; Shaw et al. 2005). However, ice crystal formation in the immediate vicinity of cloud edge by deposition cannot be ruled out. In these circumstances, ice nuclei concentration measurements using the CFDC instrument were expected to well represent all potential ice crystal nuclei concentrations. Nevertheless, comparisons using CFDC data must be viewed critically, primarily because the thermodynamic path of particles through activation was different in the CFDC than in cloud. Aerosols sampled from outside the aircraft were first heated and then underwent rapid cooling from aircraft cabin temperature to a steady-state supercooled temperature and water supersaturation in the CFDC, whereas particles entered the wave clouds already supercooled and experienced monotonically increasing RH trajectories over longer periods than the CFDC residence times.

We tested our understanding and ability to predict ice crystal formation from aerosol size distribution and composition information using a parcel model. Two different ice nucleation parameterizations that use aerosol information as input were used (PDA08 and D10). There exist other heterogeneous ice nucleation parameterizations that use aerosol information as input, but without correct constraints, these parameterizations can cause large overpredictions of heterogeneous ice nucleation (Eidhammer et al. 2009). The PDA08 parameterization requires input size distributions from dust, black carbon, and organic carbon, whereas D10 only requires information on the number concentrations of particles >0.5 μm. Both measurements and simulations indicated ice activation at similar peak water supersaturation conditions and comparable temperatures. Thus, it was expected that the modeled ice crystal concentration should be in reasonable agreement with the measurements if the connection between aerosol properties and IN activation was specified correctly.

With the initial modeling conditions taken from measurements, and using prescribed updraft velocities also deduced from measurements, we were able to reproduce many of the measured features of the cloud. The PDA08 parameterization (when using the reevaluated background dust surface area) predicted ice crystal concentrations in close agreement with IN measurements for both the dynamic trajectory modeling and the static IN concentrations calculations. The new parameterization by D10 also predicted ice crystal concentrations in good agreement with measurements.

These results offer a positive outlook on the ability of IN measurements to predict ice initiation in clouds; this should be further tested and extended to other cloud types and more complex situations. Additionally, provided that future IN measurements continue to validate the relationship among aerosol number concentrations and/or surface area concentrations and predicted ice crystal number concentrations, it is likely that for future modeling studies, measured aerosol size distributions can be used as a strong predictive link to IN concentrations in the mixed-phase regime. While including information on aerosol chemical properties should potentially lead to more accurate predictions of IN, the inclusion of chemical composition remains to be critically analyzed under a wide variety of compositional scenarios.

REFERENCES

Baker, B. A., and R. P. Lawson, 2006: In situ observations of the microphysical properties of wave, cirrus, and anvil clouds. Part I: Wave clouds. *J. Atmos. Sci.,* **63,** 3160–3185.

Baumgardner, D., R. Subramanian, C. Twohy, J. Stith, and G. Kok, 2008: Scavenging of black carbon by ice crystals over the northern Pacific. *Geophys. Res. Lett.,* **35,** L22815, doi:10.1029/2008GL035764.

Connolly, P. J., O. Möhler, P. R. Field, H. Saathoff, R. Burgess, T. Choularton, and M. Gallagher, 2009: Studies of heterogeneous freezing by three different desert dust samples. *Atmos. Chem. Phys.,* **9,** 2805–2824.

Cooper, W. A., 1986: Ice initiation in natural clouds. *Precipitation Enhancement: A Scientific Challenge, Meteor. Monogr.,* No. 43, Amer. Meteor. Soc., 29–32.

——, and G. Vali, 1981: The origin of ice in mountain cap clouds. *J. Atmos. Sci.,* **38,** 1244–1259.

Cotton, R. J., and P. R. Field, 2002: Ice nucleation characteristics of an isolated wave cloud. *Quart. J. Roy. Meteor. Soc.,* **128,** 2417–2437.

Damiani, R., and S. Haimov, 2006: A high-resolution dual-Doppler technique for fixed multiantenna airborne radar. *IEEE Trans. Geosci. Remote Sens.,* **44,** 3475–3489.

DeMott, P. J., D. J. Cziczo, A. J. Prenni, D. M. Murphy, S. M. Kreidenweis, D. S. Thomson, R. Borys, and D. C. Rogers, 2003: Measurements of the concentration and composition of nuclei for cirrus formation. *Proc. Natl. Acad. Sci. USA,* **100,** 14 655–14 660.

——, and Coauthors, 2010: Predicting global atmospheric ice nuclei distributions and their impacts on climate. *Proc. Natl. Acad. Sci. USA,* **107,** 11 217–11 222.

Diehl, K., and S. Wurzler, 2004: Heterogeneous drop freezing in the immersion mode: Model calculations considering soluble and insoluble particles in the drops. *J. Atmos. Sci.,* **61,** 2063–2072.

Drewnick, F., and Coauthors, 2005: A new time-of-flight aerosol mass spectrometer (ToF-AMS): Instrument description and first field deployment. *Aerosol Sci. Technol.,* **39,** 637–658.

Durant, A. J., and R. A. Shaw, 2005: Evaporation freezing by contact nucleation inside-out. *Geophys. Res. Lett.,* **32,** L20814, doi:10.1029/2005GL024175.

Dusek, U., G. P. Reischl, and R. Hitzenberger, 2006: CCN activation of pure and coated carbon black particles. *Environ. Sci. Technol.,* **40,** 1223–1230.

Eidhammer, T., P. J. DeMott, and S. M. Kreidenweis, 2009: A comparison of heterogeneous ice nucleation parameterizations using a parcel model framework. *J. Geophys. Res.,* **114,** D06202, doi:10.1029/2008JD011095.

Feingold, G., and A. J. Heymsfield, 1992: Parameterizations of condensational growth of droplets for use in general circulation models. *J. Atmos. Sci.,* **49,** 2325–2342.

Field, P. R., and Coauthors, 2001: Ice nucleation in orographic wave clouds: Measurements made during INTACC. *Quart. J. Roy. Meteor. Soc.,* **127,** 1493–1512.

——, R. Wood, P. R. A. Brown, P. H. Kaye, E. Hirst, and R. Greenaway, 2003: Ice particle interarrival times measured with a fast FSSP. *J. Atmos. Oceanic Technol.,* **20,** 249–261.

Fletcher, N. H., 1962: *The Physics of Rainclouds.* Cambridge University Press, 386 pp.

Fridlind, A. M., A. S. Ackerman, G. McFarquhar, G. Zhang, M. R. Poellot, P. J. DeMott, A. J. Prenni, and A. J. Heymsfield, 2007: Ice properties of single-layer stratocumulus during the Mixed-Phase Arctic Cloud Experiment (M-PACE): 2. Model results. *J. Geophys. Res.,* **112,** D24202, doi:10.1029/2007JD008646.

Hallett, J., and S. C. Mossop, 1974: Production of secondary ice particles during the riming process. *Nature,* **249,** 26–28.

Heymsfield, A. J., and L. M. Miloshevich, 1993: Homogeneous ice nucleation and supercooled liquid water in orographic wave clouds. *J. Atmos. Sci.,* **50,** 2335–2353.

Hudson, J. G., 1989: An instantaneous CCN spectrometer. *J. Atmos. Oceanic Technol.,* **6,** 1055–1065.

Jensen, E. J., and Coauthors, 2009: On the importance of small ice crystals in tropical anvil cirrus. *Atmos. Chem. Phys. Discuss.,* **9,** 5321–5370.

Khvorostyanov, V. I., and J. A. Curry, 2000: A new theory of heterogeneous ice nucleation for application in cloud and climate models. *Geophys. Res. Lett.,* **27,** 4081–4084.

——, and ——, 2004: The theory of ice nucleation by heterogeneous freezing of deliquescent mixed CCN. Part I: Critical radius, energy, and nucleation rate. *J. Atmos. Sci.,* **61,** 2676–2691.

King, W. D., D. A. Parkin, and R. J. Handsworth, 1978: A hot-wire liquid water device having fully calculable response characteristics. *J. Appl. Meteor.,* **17,** 1809–1813.

Koehler, K. A., S. M. Kreidenweis, P. J. DeMott, A. J. Prenni, and M. D. Petters, 2007: Potential impact of Owens (dry) Lake dust on warm and cold cloud formation. *J. Geophys. Res.,* **112,** D12210, doi:10.1029/2007JD008413.

Leon, D., G. Vali, and M. Lothon, 2006: Dual-Doppler analysis in a single plane from an airborne platform. *J. Atmos. Oceanic Technol.,* **23,** 3–22.

McFarquhar, G. M., J. Um, M. Freer, D. Baumgardner, G. L. Kok, and G. Mace, 2007: Importance of small ice crystals to cirrus properties: Observations from the Tropical Warm Pool International Cloud Experiment (TWP-ICE). *Geophys. Res. Lett.,* **34,** L13803, doi:10.1029/2007GL029865.

Meyers, M. P., P. J. DeMott, and W. R. Cotton, 1992: New primary ice-nucleation parameterizations in an explicit cloud model. *J. Appl. Meteor.,* **31,** 708–721.

Noone, K. J., J. A. Ogren, J. Heintzenberg, R. J. Charlson, and D. S. Covert, 1988: Design and calibration of a counterflow virtual impactor for sampling of atmospheric fog and cloud droplets. *Aerosp. Sci. Technol.,* **8,** 235–244.

Pazmany, A., R. McIntosh, R. Kelly, and G. Vali, 1994: An airborne 95-GHz dual-polarized radar for cloud studies. *IEEE Trans. Geosci. Remote Sens.,* **32,** 731–739.

Petters, M. D., and S. M. Kreidenweis, 2007: A single parameter representation of hygroscopic growth and cloud condensation nucleus activity. *Atmos. Chem. Phys.,* **7,** 1961–1971.

——, and Coauthors, 2009: Ice nuclei emissions from biomass burning. *J. Geophys. Res.,* **114,** D07209, doi:10.1029/2008JD011532.

Phillips, V. T. J., P. J. DeMott, and C. Andronache, 2008: An empirical parameterization of heterogeneous ice nucleation for multiple chemical species of aerosol. *J. Atmos. Sci.,* **65,** 2757–2783.

Pratt, K. A., and Coauthors, 2009a: Development and characterization of an aircraft aerosol time-of-flight mass spectrometer. *Anal. Chem.,* **81,** 1792–1800.

——, and Coauthors, 2009b: In-situ detection of biological particles in cloud ice-crystals. *Nat. Geosci.,* **2,** 398–401, doi:10.1038/ngeo521.

——, and Coauthors, 2010: Observation of playa salts as nuclei in orographic wave clouds. *J. Geophys. Res.,* **115,** D15301, doi:10.1029/2009JD013606.

Prenni, A. J., and Coauthors, 2007: Examinations of ice formation processes in Florida cumuli using ice nuclei measurements of anvil ice crystal particle residues. *J. Geophys. Res.,* **112,** D10221, doi:10.1029/2006JD007549.

——, M. D. Petters, A. Faulhaber, C. M. Carrico, P. J. Ziemann, S. M. Kreidenweis, and P. J. DeMott, 2009: Heterogeneous ice nucleation measurements of secondary organic aerosol generated from ozonolysis of alkenes. *Geophys. Res. Lett.,* **36,** L06808, doi:10.1029/2008GL036957.

Pruppacher, H. R., and J. D. Klett, 1997: *Microphysics of Clouds and Precipitation.* 2nd ed. Kluwer Academic, 954 pp.

Richardson, M. S., and Coauthors, 2007: Measurements of heterogeneous ice nuclei in the western United States in springtime

and their relation to aerosol characteristics. *J. Geophys. Res.,* **112,** D02209, doi:10.1029/2006JD007500.

Rogers, D. C., P. J. DeMott, S. M. Kreidenweis, and Y. L. Chen, 2001: A continuous-flow diffusion chamber for airborne measurements of ice nuclei. *J. Atmos. Oceanic Technol.,* **18,** 725–741.

Sassen, K., and G. C. Dodd, 1989: Haze particle nucleation simulation in cirrus clouds and applications for numerical and lidar studies. *J. Atmos. Sci.,* **46,** 3005–3014.

Schwarz, J. P., and Coauthors, 2006: Single-particle measurements of midlatitude black carbon and light-scattering aerosols from the boundary layer to the lower stratosphere. *J. Geophys. Res.,* **111,** D16207, doi:10.1029/2006JD007076.

Shaw, R. A., A. J. Durant, and Y. Mi, 2005: Heterogeneous surface crystallization observed in undercooled water. *J. Phys. Chem.,* **109B,** 9865–9868.

Snider, J. R., and M. D. Petters, 2008: Optical particle counter measurement of marine aerosol hygroscopic growth. *Atmos. Chem. Phys.,* **8,** 1949–1962.

Twohy, C. H., A. J. Schanot, and W. A. Cooper, 1997: Measurement of condensed water content in liquid and ice clouds using an airborne counterflow virtual impactor. *J. Atmos. Oceanic Technol.,* **14,** 197–202.

——, and Coauthors, 2010: Relationships of biomass burning aerosol to ice in orographic wave clouds. *J. Atmos. Sci.,* **67,** 2437–2450.

Vali, G., 1985: Nucleation terminology. *Bull. Amer. Meteor. Soc.,* **66,** 1426–1427.

Wang, Z., P. Wechler, W. Kuestner, J. French, A. Rodi, B. Glover, M. Burkhart, and D. Lukens, 2009: Wyoming Cloud Lidar: Instrument description and applications. *Opt. Express,* **17,** 13 576–13 587.